Experimental Validation of Constrained Spacecraft Attitude Planning via Invariant Sets

Claus Danielson *
University of New Mexico, Albuquerque, NM 87110

Joseph Kloeppel †
BlueHalo, Albuquerque, NM 87123

Christopher Petersen ‡
University of Florida, Gainesville, Fl 32611

This paper experimentally validates the invariant-set motion planner (ISMP) for the spacecraft attitude motion planning problem. Three novel results are presented that enable the experimental implementation: (i) a method for gridding quaternions from the keep-in cone, (ii) a method for scaling the invariant sets to enforce angular velocity constraints (iii) a method for scaling the sets used by the ISMP to ensure their positive invariance despite this torque constraint. The ISMP is experimentally validated through three experimental scenarios. In the first scenario, the spacecraft must perform a re-orientation maneuver that caused it to move towards a keep-out cone. The ISMP manages the momentum of the spacecraft to prevent it from overshooting into the keep-out cone. In the second scenario, the spacecraft performs a slalom maneuver to avoid a pair of keep-out cones. The ISMP must reverse the momentum of the spacecraft to transition from avoiding the first keep-out cone to the second. The final scenario is an unrealistically difficult scenario designed to stress-test the capabilities of the ISMP where the spacecraft must escape from a 'maze' of keep-out cones. These results demonstrate the ability of the ISMP to control the spacecraft attitude while enforcing state and input constraints.

*Assistant Professor, Mechanical Engineering, University of New Mexico cdanielson@unm.edu Approved for public release; distribution is unlimited. Public affairs release approval # AFRL-2023-3293

†Lead Controls and Test Engineer, BlueHalo

‡Assistant Professor, Mechanical and Aerospace Engineering Department, University of Florida

Nomenclature

$\mathbb{R}$	=	Set of reals numbers
$\bar{\mathbb{H}}$	=	Set of unitary quaternion
$\mathbb{1}$	=	Identity quaternion
$\boldsymbol{q}(t)$	=	Quaternion orientation representation
$\bar{\boldsymbol{r}}$	=	desired quaternion orientation
$\boldsymbol{e}(t) = \boldsymbol{q} \otimes \bar{\boldsymbol{r}}$	=	Error quaternion
e_0	=	Scalar part of error quaternion $\boldsymbol{e}$
$\boldsymbol{\omega}(t)$	=	Angular velocity
$\boldsymbol{\tau}(t)$	=	Torque
$\boldsymbol{q}(t) \otimes \boldsymbol{\omega}(t)$	=	Shorthand for quaternion multiplication
$\boldsymbol{J}$	=	Moment-of-Inertia matrix of satellite
$\boldsymbol{C}$	=	Output matrix
K_p	=	Proportional gain
K_d	=	Derivative gain
V	=	Lyapunov function for controller
$\mathcal{K}$	=	Avoidance cone
$\mathcal{Q}$	=	Keep-in cone
α	=	Cone Angle
$\boldsymbol{d}$	=	Unit vector in inertial frame
$\boldsymbol{b}$	=	Unit vector in body frame
$\boldsymbol{P}$	=	Matrix for quadratic form of cone constraints
Ω	=	Angular velocity constraint set
$\boldsymbol{W}$	=	Matrix defining ellipsoidal inner-approximation of angular velocity constraints

$\boldsymbol{u}$ = Actuator command

n_u = Number of actuators

$\mathcal{U}$ = Actuator constraint set

$\mathcal{T}$ = Torque constraint set

$\bar{\mathcal{T}}$ = Inner-approximation for torque constraint

$\boldsymbol{T}$ = Control-actuator matrix relating actuator commands $\boldsymbol{u}$ to torques $\boldsymbol{\tau}$

$\mathbb{G}$ = Search graph / network

$\mathbb{I}$ = Set of graph nodes

$\mathbb{E}$ = Set of graph edges

σ_i = Sequence of indices of planned references

$\mathcal{O}$ = Positively invariant set

ρ = Lyapunov level set tunning parameter

$\cdot^\times$ = Skew symmetric matrix operator

I. Introduction

The objective of the spacecraft constrained attitude motion-planning problem is to rotate the spacecraft into a desired orientation while enforcing angular velocity constraints and avoiding undesirable orientations despite limited control authority. This problem has been address through a variety of approaches including ground-based human-in-the-loop planning, as opposed to the autonomous approach proposed in this paper. See [1] for a classical survey of solutions to the constrained attitude motion planning problem. Artificial potential functions [2–8] are one popular solution to this problem since they exploit well-known Lyapunov theory and provide rapid implementation, although they can inadvertently produce spurious equilbria causing the spacecraft to become trapped in an undesired orientation. Another popular approach are optimization-based methods which leverage popular numerical solvers to optimize performance, but often suffer from high computational costs [9–15]. This paper employs another popular approach in which the attitude-space is discretized and searched using graph search methods [16–20]. The challenge with this approach is ensuring constraint satisfaction between waypoints despite imperfect reference tracking. This paper addresses this problem using the invariant-set motion-planner (ISMP) to ensure constraint satisfaction despite imperfect tracking. All these techniques have advantages and disadvantages, and a framework to compare some of these was presented in [21]. While the method of this paper share commonalities with the discretization and optimization-based methods, it stands apart by uniquely blending the theoretic aspects of positive invariant sets and numeric structure of the constraints to

quickly and reliably construct a safe constrained attitude path.

This paper experimentally validates the ISMP for the spacecraft constrianed attitude motion planning problem. The ISMP generates a sequence of reference waypoints to safely guide a closed-loop dynamical system from an initial state to a target equilibrium through an obstacle-filled environment despite limited control authority [22–33]. Like other motion-planning algorithms, such as rapidly-exploring random trees (RRT) [34, 35], the ISMP abstracts the motion-planning problem as a graph search. The defining feature of the ISMP is that knowledge of the closed-loop system dynamics is incorporated into the search graph using constraint admissible positive invariant (CAPI) sets (also called viable sets [36]). These CAPI sets describe regions of the state-space where the closed-loop system dynamics will safely track the corresponding reference despite imperfect tracking. The ISMP uses a graph search to find a corridor of CAPI sets that safely guides the system through the obstacle filled environment to the target equilibrium.

The ISMP has several advantageous properties. It allows for aggressive, but safe maneuvers since, by definition, the system state will never leave the CAPI sets. It is inherently robust to model uncertainty and disturbances [27] since it incorporates feedback into the design and the CAPI sets provide a natural buffer that can absorb tracking errors. It typically has low online computational costs since the CAPI sets can be pre-computed as they only depend on the time-invariant closed-loop dynamics, rather than the time varying environment. Furthermore, it reduces the curse-of-dimensionality by sampling from the output-space instead of the state-space. Indeed for this paper, we sample the orientation-space (quaternions) rather than the full state-space, which also includes the spacecraft angular velocity. Since it plans motion based on the closed-loop dynamics, the ISMP does not require replacing the existing controller with a customized controller. Indeed, we leverage a standard quaternion-based proportional-derivative controller for reference tracking.

In our previous work [32], we applied the ISMP to spacecraft controlled by quaternion-based state-feedback controllers. The main contribution of [32] was a closed-form solution for certifying the safety of the CAPI sets. That paper [32] focused on the computational aspects of the safety test. Only a single *simulation* was presented that provided minimal insight into the advantages of the ISMP for spacecraft attitude motion planning. In contrast, the main contribution of this paper is an in-depth *experimental* validation of the ISMP for spacecraft attitude planning. Experimental validation was conducted using the Air Force Research Laboratory (AFRL) Space Vehicles Directorate's large spherical air-bearing spacecraft simulator [37, 38]. The experiments used existing systems on the ReBEL testbed without need for specialized hardware or software. The experiments make use of the existing steering-law for allocating actuator commands to achieve the desired torque.

Terrestrial experiments are an important tool for the validation of space technology since accessibility to the space-domain is limited due to launch availability, high financial costs, and a traditionally risk adverse environment. To bring new technologies as close to flight-readiness as possible, there are a number of terresital experimental systems that can be employed. Ground robotics can demonstrate algorithms on embedded systems [39], but are often restricted to 3

degrees of motion (2 translational, 1 rotational) and are always fighting friction when tracking approximated satellite dynamics. Drones can obtain 6 degrees of motion [40, 41], but due to actuator placement and limitations, cannot perform certain maneuvers, e.g. a quadcopter cannot flip upside down and still hover. In addition, their actuators are not representative of spacecraft and thus they are also forced to track approximated spacecraft dynamics. Platforms exploiting air-bearing mechanisms [42, 43] enable near frictonless environments that can successfully emulate spacecraft motion with representative actuators (e.g., air thrusters) but are also limited in their motion due to air-bearing placement. Although none of these platforms perfectly emulates space, it is important to test new algorithms on an experimental testbed that is partially representative of a real spacecraft in order to reduce risk before deployment in the space domain.

We present the results of three experimental scenarios that demonstrate the advantages of incorporating knowledge of the spacecraft dynamics into the motion planning problem. The first experimental scenario is a pointing maneuver where the spacecraft is commanded to rotate to a target orientation near the edge of a keep-out cone. The ISMP must anticipate the momentum of the spacecraft to avoid overshoot that would carry the spacecraft into the keep-out cone. The second experimental scenario is a slalom maneuver. In this scenario the spacecraft is rotating about its x-axis to a target orientation while simultaneously rotating about the y-axis to avoid keep-out cones. The spacecraft must first rotate in the positive y-direction to avoid the first keep-out cone and then reverse its momentum to rotation in the negative y-direction to avoid the second keep-out cone. In the final experimental scenario, the spacecraft must navigate out of a 'maze' of keep-out cones. This unrealistically challenging scenario is meant to stress-test the ISMP algorithm and its ability to enforce state and input constraints. Together, these three experimental results demonstrate the ability of the ISMP to safely navigate the spacecraft attitude around undesirable orientations to a desired equilibrium.

In addition to the experimental results, we present novel theoretical results developed to enable the experimental implementation of our algorithm. Since our experimental platform has a severe keep-in cone constraint, we develop a novel method for gridding quaternions that satisfy the keep-in cone constraints. This reduces memory usage by only sampling orientations from the keep-in cone rather than sampling the entire orientation space and rejecting unsafe orientations. This allows us to only plan maneuvers that respect the safe operating conditions for our experimental setup. In practice, this parameterization of a keep-in cone could be used to ensure that the solar panels on a spacecraft are always oriented to gather sufficient sunlight. This paper contributes a novel method for scaling our invariant sets to enforce constraints on the angular velocity of the spacecraft and the torque provided by the actuators. Enforcing angular velocity constraints is important because the experimental platform has a large inertia. At high angular velocities, this will produce a large angular moment which the emergency shut-down systems will not be able to absorb. In practice, enforcing angular velocity constraints is important because it ensures safety of certain spacecraft components and subsystems. For example, if a solar panel is attached to the satellite, rotating at a high angular velocity could excite flexible modes that could harm the spacecraft or its components. In addition, if the satellite is rotating too quickly, the solar panel may not be able to absorb enough power, resulting in insufficient power for the system to complete its

mission. Enforcing input constraints is important to ensure that the ISMP does not require steering torques that are physically unrealizable by the experimental platform. Indeed, one of the main advantages of the ISMP is that it can manage the momemtum of the spacecraft to avoid obstacles despite limited control authority. Another advantage is the opportunity to leverage advanced steering laws such as a triplet steering-law to allocate torques to the 6 control moment gryo (CMG)s to ensure that a minimal torque envelop is always available. In practice, enforcing torque constraints is important since actual spacecraft actuators will have limitations on their control authority.

The remainder of this paper is organized as follows. In Section II, we describe the spacecraft constrained attitude planning problem. In Section III, we describe the ISMP for spacecraft attitude control, including the constraint admissible positive invariant set and search graph construction. In Section IV, we present three experimental results that demonstrates advantages of the ISMP for spacecraft attitude motion planning.

II. Spacecraft Attitude Motion-Planning Problem

In this section, we describe the dynamics and constraints that define the spacecraft constrained attitude motion planning problem.

A. Spacecraft Attitude Dynamics

The spacecraft attitude dynamics are modeled by

$$\dot{\boldsymbol{q}}(t) = \tfrac{1}{2}\boldsymbol{q}(t) \otimes \boldsymbol{\omega}(t) \tag{1a}$$

$$\boldsymbol{J}\dot{\boldsymbol{\omega}}(t) = -\boldsymbol{\omega}(t) \times \boldsymbol{J}\boldsymbol{\omega}(t) + \boldsymbol{\tau}(t) \tag{1b}$$

where $\boldsymbol{q} \in \bar{\mathbb{H}}$ and $\boldsymbol{\omega} \in \mathbb{R}^3$ are the spacecraft orientation and angular velocity, respectively, $\boldsymbol{\tau} \in \mathbb{R}^3$ is the torque applied to the spacecraft attitude, and $\boldsymbol{J} \in \mathbb{R}^{3\times3}$ is the spacecraft moment-of-inertia matrix. With abuse of notation, $\boldsymbol{q}(t) \otimes \boldsymbol{\omega}(t)$ is shorthand for the quaternion multiplication $\boldsymbol{q}(t) \otimes (0, \boldsymbol{\omega}(t))$ The output-matrix $\boldsymbol{C} = [I_4, 0] \in \mathbb{R}^{4\times7}$ extracts the orientation $\boldsymbol{q} = \boldsymbol{C}\boldsymbol{x} \in \bar{\mathbb{H}}$ from the state $\boldsymbol{x} = (\boldsymbol{q}, \boldsymbol{\omega}) \in \bar{\mathbb{H}} \times \mathbb{R}^3$.

The orientation of the spacecraft is controlled by a standard proportional-derivative quaternion attitude controller [44]

$$\boldsymbol{\tau}(t) = \boldsymbol{\omega}(t) \times \boldsymbol{J}\boldsymbol{\omega}(t) - K_p e_v(t) - K_d\boldsymbol{\omega}(t) \tag{1c}$$

where the error-quaternion $\boldsymbol{e}(t) = \pm\boldsymbol{q}(t) \otimes \boldsymbol{r} \in \bar{\mathbb{H}}$ between the actual $\boldsymbol{q}(t) \in \bar{\mathbb{H}}$ and desired $\boldsymbol{r} \in \bar{\mathbb{H}}$ orientations of the spacecraft is chosen such that scalar part $e_0 = \pm\boldsymbol{q}^\top\boldsymbol{r} \geq 0$ is non-negative where the quaternions $\bar{\mathbb{H}}$ are a double-cover of $\mathbb{SO}(3)$. The proportional and derivative gains of the controller are $K_p = k_p\boldsymbol{I} \in \mathbb{R}^{3\times3}$ and $K_d \in \mathbb{R}^{3\times3}$, respectively, where K_d satisfies the Lyapunov equation $\boldsymbol{J}^{-1}K_d + K_d\boldsymbol{J}^{-1} \prec 0$. The robustness [45] and boundedness [46] of the

closed-loop dynamics (1) have been previously studied. A torque allocation law computes actuators commands to supply the desired torque $\boldsymbol{\tau}(t)$ e.g. from electromagnetic torque rods, thrusters, reaction wheels, or control moment gyroscopes. This is discussed further in Section II.B.4.

The asymptotic stability of the equilibrium $(\boldsymbol{e}, \boldsymbol{\omega}) = (0, 0)$ for the closed-loop system (1) is certified by the following Lyapunov function [47, 48]

$$V(\boldsymbol{e}, \boldsymbol{\omega}) = \begin{bmatrix} \boldsymbol{e} - \mathbb{1} \\ \boldsymbol{\omega} \end{bmatrix}^\top \begin{bmatrix} \boldsymbol{I} & 0 \\ 0 & k_p^{-1}\boldsymbol{I} \end{bmatrix} \begin{bmatrix} \boldsymbol{e} - \mathbb{1} \\ \boldsymbol{\omega} \end{bmatrix} = 2 - 2e_0 + k_p^{-1}\|\boldsymbol{\omega}\|^2 \tag{2}$$

where $\mathbb{1} \in \bar{\mathbb{H}}$ is the identity quaternion and $e_0 = \pm \boldsymbol{q}^\top \boldsymbol{r} \geq 0$. Since $\boldsymbol{e}$ is a unit quaternion, the identity $\boldsymbol{e}^\top \boldsymbol{e} = 1$ can be used to simplify the Lyapunov function into the second equality [32]. The invariant-set motion-planner will use the Lyapunov function (2) to plan safe re-orientation maneuvers.

B. Spacecraft Constraints

In this section, we describe the constraints on the spacecraft attitude $\boldsymbol{q}$, angular velocity $\boldsymbol{\omega}$, and torque $\boldsymbol{\tau}$.

1. Attitude Keep-Out Cones

Keep-out cones are a common type of output constraints in which the spacecraft orientation $\boldsymbol{q}(t)$ must be kept out $\boldsymbol{q}(t) \notin \mathcal{K} \subseteq \bar{\mathbb{H}}$ of the cone

$$\mathcal{K}(\boldsymbol{d}, \boldsymbol{b}, \alpha) = \left\{ \boldsymbol{q} \in \bar{\mathbb{H}} : \boldsymbol{d}^\top \boldsymbol{R}(\boldsymbol{q}) \boldsymbol{b} \geq \cos(\alpha) \right\} = \left\{ \boldsymbol{q} \in \bar{\mathbb{H}} : \boldsymbol{q}^\top \boldsymbol{P} \boldsymbol{q} \geq \cos \alpha \right\} \tag{3}$$

where α is the cone angle, $\boldsymbol{d} \in \mathbb{S}^2$ and $\boldsymbol{b} \in \mathbb{S}^2$ are unit-vectors in the inertial and body frames, respectively, and $\boldsymbol{R}(\boldsymbol{q})$ is the rotation-matrix between these frames, which depends on the spacecraft orientation $\boldsymbol{q} \in \bar{\mathbb{H}}$. The constraint $\boldsymbol{q}(t) \notin \mathcal{K}$ keeps the angle $\cos^{-1}(\boldsymbol{d}^\top \boldsymbol{R}(\boldsymbol{q}) \boldsymbol{b})$ between the inertial-frame $\boldsymbol{d}$ and body-frame $\boldsymbol{b}$ unit-vectors sufficiently large $\cos^{-1}(\boldsymbol{d}^\top \boldsymbol{R}(\boldsymbol{q}) \boldsymbol{b}) > \alpha$. Keep-out constraints can be used to ensure that a sensitive onboard instrument (e.g. a star-tracker) is not pointed at a bright object (e.g. the sun, earth, or moon) which could temporarily blind or even permanently damage the instrument. Likewise, a keep-out constraint could be used to prevent a spacecraft from pointing its thrust at a nearby object during proximity operations. Equivalently, the keep-out cone (3) can be written as a quadratic-form $\boldsymbol{q}^\top \boldsymbol{P} \boldsymbol{q} \geq \cos \alpha$ of the quaternion $\boldsymbol{q}$ [32] where

$$\boldsymbol{P} = \begin{bmatrix} \boldsymbol{d}^\top \boldsymbol{b} & -(\boldsymbol{d} \times \boldsymbol{b})^\top \\ -\boldsymbol{d} \times \boldsymbol{b} & \boldsymbol{d}\boldsymbol{b}^\top + \boldsymbol{b}\boldsymbol{d}^\top - \boldsymbol{d}^\top \boldsymbol{b} \boldsymbol{I} \end{bmatrix}. \tag{4}$$

We will use this second description of the keep-out cone (3) and properties of the matrix (4) to enforce safety constraints.

2. Attitude Keep-In Cones

Keep-in cones are another common type of output constraints in which the spacecraft orientation $\boldsymbol{q}(t)$ must be kept inside $\boldsymbol{q}(t) \in \mathcal{Q}$ a cone

$$\mathcal{Q} = \left\{ \boldsymbol{q} \in \bar{\mathbb{H}} : \boldsymbol{d}_{\mathcal{Q}}^{\top} \boldsymbol{R}(\boldsymbol{q}) \boldsymbol{b} > \cos \alpha_{\mathcal{Q}} \right\}. \tag{5}$$

Keep-in constraints ensure that the body-frame $\boldsymbol{b} \in \mathbb{S}^2$ and inertia-frame $\boldsymbol{d}_{\mathcal{Q}} \in \mathbb{S}^2$ vectors are aligned $\boldsymbol{d}^{\top} \boldsymbol{R}(\boldsymbol{q}) \boldsymbol{b} \geq \cos \alpha_{\mathcal{Q}}$. For instance, a keep-in constraints can be used to ensure that the solar panels receive sufficient sun-light or an onboard instrument (e.g. a telescope) point in a particular direction. Keep-in constraints are mathematically equivalent to enforcing keep-out constraints $\boldsymbol{q}(t) \notin \bar{\mathbb{H}} \backslash \mathcal{Q}$ on the complement $\mathcal{K} = \bar{\mathbb{H}} \backslash \mathcal{Q}$ of the keep-in set $\mathcal{Q}$. Note that the complement $\bar{\mathbb{H}} \setminus \mathcal{Q}$ has the form (3) where $\boldsymbol{d} = -\boldsymbol{d}_{\mathcal{Q}}$ and $\theta = \pi - \alpha_{\mathcal{Q}}$. Thus, the keep-in cone constraint $\boldsymbol{d}^{\top} \boldsymbol{R}(\boldsymbol{q}) \boldsymbol{b} \geq \cos \alpha_{\mathcal{Q}}$ can be written as a quadratic constraints $\boldsymbol{q}^{\top} \boldsymbol{P} \boldsymbol{q}$ on the quaternion where $\boldsymbol{P} \in \mathbb{R}^{4 \times 4}$ has the form (4) with $\boldsymbol{d}$ replaced by $\boldsymbol{d}_{\mathcal{Q}}$.

Although they are mathematically equivalent, we will treat keep-in cones differently from keep-out cones in this paper. In particular, we will present a method for parameterizing quaternions that satisfy the keep-in cone constraints to allow efficient gridding of the keep-in cone.

3. Angular Velocity Constraints

The angular velocity of the spacecraft may also be constrained. For our experiments, the angular velocity must be limited to prevent dangerously large angular momentum which could overwhelm the safety system and damage the experimental platform. In practice, the angular velocity may be limited to ensure the safety of certain spacecraft components and subsystems or to ensure that the satellite is kept in a power positive configuration (i.e., solar panels are always mostly exposed to the sun for a long duration of time). We assume that the angular velocity constraint set $\Omega \subseteq \mathbb{R}^3$ contains the origin in its interior so that the spacecraft is allowed to have a small angular velocity in any direction.

4. Torque and Input Constraints

We assume that the torque is constrained $\boldsymbol{\tau} \in \mathcal{T}$ to a set $\mathcal{T} \subseteq \mathbb{R}^3$ which contains a neighborhood of the origin. This ensures that the controller (1c) can produce a small torque $\boldsymbol{\tau} \in \mathcal{T}$ in any direction. This requirement is complicated by the fact that the torque $\boldsymbol{\tau}$ is not the control input. Rather, the commands to the actuators (thrusters, reaction wheels, CMGs, torque-rods) are the control inputs. A torque allocation law maps the torque $\boldsymbol{\tau} \in \mathbb{R}^3$ requested by the controller (1c) to an actuator command $\boldsymbol{u} \in \mathbb{R}^{n_u}$ that realizes this torque. For most types of actuators (not CMGs), this distinction is inconsequential. The input and torque can be related $\boldsymbol{\tau} = \boldsymbol{T}\boldsymbol{u}$ by a fixed matrix $\boldsymbol{T} \in \mathbb{R}^{3 \times n_u}$ where n_u is the number of actuators. For instance, the columns of $\boldsymbol{T}$ can indicate the spin-axis and moments-of-inertia of reaction wheels. For

a fully-actuated spacecraft, this matrix $\boldsymbol{T}$ is full-rank. Thus, if the actuator constraints $\mathcal{U}$ contain the origin in their interior then the torque set $\mathcal{T} = \boldsymbol{T}\mathcal{U} = \{Tu : \boldsymbol{u} \in \mathcal{U}\}$ will as well [49].

For CMGs, the matrix $\boldsymbol{T}(\delta) \in \mathbb{R}^{3\times n_u}$ is time-varying since it depends on the time-varying gimbal angles $\dot{\delta}(t) = \boldsymbol{u}(t)$ of the CMGs which integrate the input $\boldsymbol{u}(t)$ history. It is well-known that a poorly designed torque allocation law can drive the CMGs into a singular configuration where the matrix $\boldsymbol{T}$ loses rank [37]. Therefore, it is important to use a CMG torque allocation law (also known as a steering law) which guarantees $\boldsymbol{T}$ is full-rank and thus $\mathcal{T} = \boldsymbol{T}\mathcal{U}$ contains the origin in its interior. Mathematically, this ensures that singularity can be escaped with zero torque error, even if it takes more control effort. Practically, what this entails is even if the CMGs results in a singular configuration, it can exit it with zero torque error. A common example of this is if a pair of CMGs have their gimbal axes aligned and are in singularity, they can perform a "scissor"-like maneuver by aligning their angular momentum axes for a certain period of time and escape. See [37] for more examples. A properly designed steering law can enforce a lower-bound on the minimum spectral-norm $\|\boldsymbol{T}(\delta)\|_2$ of the matrix $\boldsymbol{T}(\delta)$ [50, 51].

C. Spacecraft Attitude Motion Planning Problem

In this section, we summarize the spacecraft attitude motion planning problem.

Problem 1 *Find a feasible torque trajectory $\boldsymbol{\tau}(t) \in \mathcal{T}(t)$ such that the resulting angular velocity satisfies its constraints $\boldsymbol{\omega}(t) \in \Omega$ and the spacecraft orientation satisfies its constraints $\boldsymbol{q}(t) \in \mathcal{Q}$ and $\boldsymbol{q}(t) \notin \mathcal{K}_k$ and converges to the target orientation $\boldsymbol{q}(t) \to \boldsymbol{r}_\infty$ as $t \to \infty$.* □

In the next section, we present the ISMP algorithm for solving this problem.

III. Invariant-Set Motion-Planning Algorithm

The ISMP is an algorithm for solving motion planning problems, such as Problem 1. The ISMP is described by Algorithm 1. The ISMP searches an appropriately constructed directed graph $\mathbb{G}$ for a sequence $\{\bar{\boldsymbol{r}}_i\}_{i=1}^N$ of intermediate reference orientations $\bar{\boldsymbol{r}}_i \in \bar{\mathbb{H}}$ that guide the spacecraft (1) state $\boldsymbol{x}(t) = (\boldsymbol{q}(t), \boldsymbol{\omega}(t)) \in \bar{\mathbb{H}} \times \mathbb{R}^3$ from an initial state $(\boldsymbol{q}(0), \boldsymbol{\omega}(0))$ to a target equilibrium orientation $(\boldsymbol{r}_\infty, 0) \in \bar{\mathbb{H}} \times \mathbb{R}^3$ while enforcing state and input constraints such as keep-out cone $\boldsymbol{q}(t) = \boldsymbol{C}\boldsymbol{x}(t) \notin \mathcal{K}_k$ and keep-in cone constraints $\boldsymbol{q}(t) = \boldsymbol{C}\boldsymbol{x}(t) \in \mathcal{Q}_k$. The distinguishing feature of the ISMP is that knowledge of the closed-loop spacecraft dynamics (1) is incorporated into the graph $\mathbb{G}$ using its CAPI sets. Associated with each node $i \in \mathbb{I}$ is a set $\mathcal{O}_i$, which is constraint admissible $\boldsymbol{C}\mathcal{O}_i \cap \mathcal{K}_k = \varnothing$ and positive invariant $\boldsymbol{x}(0) \in \mathcal{O}_i \Rightarrow \boldsymbol{x}(t) \in \mathcal{O}_i \ \forall t > 0$. Since the set $\mathcal{O}_i$ is constraint admissible, it does not collide with an obstacle e.g. keep-out cone. Since the set $\mathcal{O}_i$ is positive invariant, the state $\boldsymbol{x}(t) \in \mathcal{O}_i$ will remain in the set while tracking the reference orientation $\boldsymbol{r}_i \in \bar{\mathbb{H}}$. The edges $(i, j) \in \mathbb{E}$ of the graph $\mathbb{G} = (\mathbb{I}, \mathbb{E})$ indicate that the state (1) will enter the j-th safe-set $\mathcal{O}_j$ while tracking the i-th node without leaving the current safe-set $\mathcal{O}_i$. Once the state $\boldsymbol{x}(t)$ enters the next set

$\mathcal{O}_j$, it can safely switch to tracking the next reference $\boldsymbol{r}_j$. Thus, the ISMP avoids obstacles by moving the closed-loop spacecraft state $(\boldsymbol{q}(t), \boldsymbol{\omega}(t)) \in \bar{\mathbb{H}} \times \mathbb{R}^3$ through a sequence of safe CAPI sets $\mathcal{O}_{\sigma_i}$ for $\{\sigma_i\}_{i=0}^N$.

Algorithm 1 Invariant-Set Motion-Planner

1: Remove unsafe $\boldsymbol{CO}_i \cap \mathcal{K}_k \neq \varnothing$ nodes $i \in \mathbb{I}$ from $\mathbb{G}$
2: Search the graph $\mathbb{G}$ for a path $\{\boldsymbol{r}_{\sigma_0}, \ldots, \boldsymbol{r}_{\sigma_N}\}$ from $\boldsymbol{r}_{\sigma_0} = \boldsymbol{q}(0)$ to $\boldsymbol{r}_{\sigma_N} = \boldsymbol{r}_\infty$
3: Set $k \leftarrow 0$
4: **repeat**
5: **if** $\boldsymbol{x}(t) \in \mathcal{O}_{\sigma_{k+1}}$ **then**
6: $k \leftarrow k + 1$
7: **end if**
8: track current target state $\boldsymbol{r}(t) = \boldsymbol{r}_{\sigma_k}$
9: **until** $\boldsymbol{r}(t) = \boldsymbol{r}_\infty$

This paper applies the ISMP to the problem of spacecraft constrained attitude control. In this section, we will describe CAPI sets $\mathcal{O}$ for spacecraft closed-loop dynamics (1). We will describe the necessary and sufficient condition for certifying the safety of these sets (output admissibility). Then, we will describe how to scale these sets to enforce angular velocity and torque constraints (input admissibilty). Finally, we will describe how to construct the search-graph $\mathbb{G} = (\mathbb{I}, \mathbb{E})$ by sampling the reference orientations $\boldsymbol{r}_i$ for $i \in \mathbb{I}$ and safely connected these nodes $(i, j) \in \mathbb{E}$.

A. Invariant-Sets

Level-sets of the Lyapunov function (2) are positive invariant (PI) sets $\mathcal{O}_i$ of the closed-loop system (1)

$$\mathcal{O}(\boldsymbol{r}, \rho) = \left\{ \begin{bmatrix} \boldsymbol{q} \\ \boldsymbol{\omega} \end{bmatrix} \in \bar{\mathbb{H}} \times \mathbb{R}^3 : 2 - 2\boldsymbol{q}^\top \boldsymbol{r} + \boldsymbol{\omega}^\top K_p^{-1} \boldsymbol{J} \boldsymbol{\omega} \leq \rho^2 \right\} \tag{6}$$

where $e_0 = |\boldsymbol{q}^\top \bar{\boldsymbol{r}}|$ is the scalar-part of the error-quaternion $\boldsymbol{e} = \pm \boldsymbol{q} \otimes \boldsymbol{r}$, $\boldsymbol{r} \in \bar{\mathbb{H}}$ is the reference orientation for the PI set, and $\bar{\boldsymbol{r}} \in \bar{\mathbb{H}}$ is its conjugate. The level $\rho^2 \in (0, 2)$ of the Lyapunov function (2) is a tuning parameter that will be used in the graph $\mathbb{G}$ construction as well as enforcement of the angular velocity and torque constraints.

1. Safety Certification

Line 1 of Algorithm 1 requires the removal of unsafe nodes $\boldsymbol{CO}_i \cap \mathcal{K}_k \neq \varnothing$ from the search graph. In other words, we must remove PI sets $\mathcal{O}_i$ that are not output admissible. A computationally efficient method for detecting collisions $\boldsymbol{CO}_i \cap \mathcal{K}_k \neq \varnothing$ was presented in [32]. This method is summarized by the following Theorem.

Theorem 1 (Output Admissibility) *A PI set* (6) *is safe* $\boldsymbol{CO}(\boldsymbol{r},\rho)\cap\mathcal{K}(\boldsymbol{d},\boldsymbol{b},\alpha)=\varnothing$ *if and only if* $\|\boldsymbol{P}_+\boldsymbol{r}\|=0$ *or*

$$\|\boldsymbol{P}_+\boldsymbol{r}\|\leq 1-\tfrac{1}{2}\rho^2 \qquad \textit{and} \qquad \begin{bmatrix} 1-\frac{1}{2}\rho^2 \\ 2\rho\sqrt{4-\rho^2}\end{bmatrix}^\top \begin{bmatrix}\|\boldsymbol{P}_+\boldsymbol{r}\| \\ \|\boldsymbol{P}_-\boldsymbol{r}\|\end{bmatrix} \leq \sqrt{\frac{1}{2}+\frac{1}{2}\cos(\alpha)} \tag{7}$$

where

$$\boldsymbol{P}_+=\frac{1}{\sqrt{2+2\boldsymbol{d}^\top\boldsymbol{b}}}\begin{bmatrix}0 & 1+\boldsymbol{d}^\top\boldsymbol{b}\\ \boldsymbol{d}+\boldsymbol{b} & -\boldsymbol{d}\times\boldsymbol{b}\end{bmatrix}\in\mathbb{R}^{4\times 2} \textit{ and } \boldsymbol{P}_-=\frac{1}{\sqrt{2-2\boldsymbol{d}^\top\boldsymbol{b}}}\begin{bmatrix}0 & 1-\boldsymbol{d}^\top\boldsymbol{b}\\ \boldsymbol{d}-\boldsymbol{b} & \boldsymbol{d}\times\boldsymbol{b}\end{bmatrix}\in\mathbb{R}^{4\times 2}. \tag{8}$$

The proof is provided in [32]. Theorem 1 provides the necessary and sufficient conditions for safety $\boldsymbol{CO}\cap\mathcal{K}\neq\varnothing$.

The collision detection (7) is computationally inexpensive since it only requires checking the inner-product of vectors in $\mathbb{R}^2$. Furthermore, for each keep-out cone $\mathcal{K}(\boldsymbol{d},\boldsymbol{b},\alpha)$, the safety test (7) can be vectorized to simultaneously checked all the PI sets $\boldsymbol{O}(\boldsymbol{r}_i,\rho_i)$ for $i\in\mathbb{I}$.

2. Angular Velocity Constraint Enforcement

The angular velocity constraints $\Omega\subseteq\mathbb{R}^3$ are enforced by setting a maximum level $\rho^2\in(0,2)$ for the PI set (6). From the definition of the PI set (6), the angular velocity $\boldsymbol{\omega}$ is bounded $\|\boldsymbol{\omega}\|^2\leq k_p\rho^2$. Thus, if the angular velocity constraint set Ω is inner-approximated by an ellipsoid $\{\boldsymbol{\omega}:\boldsymbol{\omega}^\top\boldsymbol{W}\boldsymbol{\omega}\leq 1\}\subseteq\Omega$ then $\rho^2\leq\|\boldsymbol{W}\|_2/k_p$ will ensure the satisfaction of the angular velocity constraints where $\|\boldsymbol{W}\|_2$ is the induced 2-norm of the matrix $\boldsymbol{W}$. Likewise, if the angular velocity constraint set Ω is inner-approximated by a polyhedron $\{\boldsymbol{\omega}:w_j\boldsymbol{\omega}\leq 1,j=1,\ldots,m\}\subseteq\Omega$ then $\rho^2\leq\|w_j\|^2/k_p$ will ensure that the angular velocity constraint are satisfied.

3. Torque Constraint Enforcement

Like angular velocity, the torque constraints $\mathcal{T}=\boldsymbol{T}\mathcal{U}$ are enforce by setting a maximum level $\rho^2\in(0,2)$ for the PI set (6). The following proposition describes two methods for bounding the level to ensure input admissibility.

Proposition 1 (Input Admissibility)

- *If* $\mathcal{T}$ *is inner-approximated by an ellipsoidal set* $\{\boldsymbol{\tau}:\|H\boldsymbol{\tau}\|\leq 1\}\subseteq\mathcal{T}$ *then the input constraints are satisfied for*

$$\rho\leq\frac{\left\|H(k_p\boldsymbol{I}+\sqrt{k_p}K_d)\right\|+\sqrt{\left\|H(k_p\boldsymbol{I}+\sqrt{k_p}K_d)\right\|^2+\|H\|_2\|\boldsymbol{J}\|_2}}{2\|\boldsymbol{J}\|_2\|H\|_2}. \tag{9a}$$

- *If* $\mathcal{T}$ *is inner-approximated by a polytopic set* $\{\boldsymbol{\tau}:\pm h_j\boldsymbol{\tau}\leq 1,j=1,\ldots,m\}\subseteq\mathcal{T}$ *then the input constraints are*

satisfied for

$$\rho \leq \min_{j=1,\ldots,m} \frac{\left\|h_j(k_p\boldsymbol{I}+\sqrt{k_p}K_d)\right\| + \sqrt{\left\|h_j(k_p\boldsymbol{I}+\sqrt{k_p}K_d)\right\|^2 + \|h_j\|_2\|\boldsymbol{J}\|_2}}{2\|\boldsymbol{J}\|_2\|h_j\|_2}. \tag{9b}$$

Proof: The PI set (6) is input admissible if the maximum torque produce by the nonlinear state-feedback controller (1c) over the subset of states (6) satisfies the ellipsoidal torque constraints $\mathcal{T} = \left\{\boldsymbol{\tau} : \|H\boldsymbol{\tau}\| \leq 1\right\}$ i.e.

$$\max_{(\boldsymbol{e},\boldsymbol{\omega})\in O} \|H(K_p e_v + K_d\boldsymbol{\omega} + \boldsymbol{\omega}\times\boldsymbol{J}\boldsymbol{\omega})\| \leq 1.$$

By the triangle inequality and definition of the maximum operator, we have

$$\max_{(\boldsymbol{e},\boldsymbol{\omega})\in O} \|H\boldsymbol{\tau}\| \leq \max_{(\boldsymbol{e},\boldsymbol{\omega})\in O} \|HK_p e_v + HK_d\boldsymbol{\omega}\| + \max_{(\boldsymbol{e},\boldsymbol{\omega})\in O} \|H\boldsymbol{\omega}\times\boldsymbol{J}\boldsymbol{\omega}\|$$

where the first-term is the linear part of the controller (1c) and the second-term is the nonlinear Coriolis cancellation. The first-term can be bounded using the definition of the spectral-norm of a matrix

$$\max_{(\boldsymbol{e},\boldsymbol{\omega})\in O} \|HK_p e_v + HK_d\boldsymbol{\omega}\| = \max_{(\boldsymbol{e},\boldsymbol{\omega})\in O} \left\| \begin{bmatrix} k_p H & \sqrt{k_p}HK_d \end{bmatrix} \begin{bmatrix} e_v \\ \boldsymbol{\omega}/\sqrt{k_p} \end{bmatrix} \right\| = \left\| \begin{bmatrix} k_p H & \sqrt{k_p}HK_d \end{bmatrix} \right\|$$

where $\|e_v\|^2 + k_p^{-1}\|\boldsymbol{\omega}\|^2 \leq 1$ for all $(\boldsymbol{e},\boldsymbol{\omega}) \in O$. The second-term can be bounded by $\|H\boldsymbol{\omega}\times\boldsymbol{J}\boldsymbol{\omega}\| \leq \|H\|_2\|\boldsymbol{J}\|_2\|\boldsymbol{\omega}\|_2^2$. Thus,

$$\max_{(\boldsymbol{e},\boldsymbol{\omega})\in O} \|H\boldsymbol{\tau}\| \leq \rho\left\|H(k_p\boldsymbol{I}+\sqrt{k_p}K_d)\right\| + \rho^2\|\boldsymbol{J}\|_2\|H\|_2.$$

Therefore, the PI set (6) is input admissible $\max \|H\boldsymbol{\tau}\| \leq 1$ if the following quadratic inequality holds

$$\rho^2\|\boldsymbol{J}\|_2\|H\|_2 + \rho\left\|H(k_p\boldsymbol{I}+\sqrt{k_p}K_d)\right\| - 1 \leq 0$$

Since this quadratic equation is convex, it is negative between its roots

$$\rho \in \frac{\left\|H(k_p\boldsymbol{I}+\sqrt{k_p}K_d)\right\| \pm \sqrt{\left\|H(k_p\boldsymbol{I}+\sqrt{k_p}K_d)\right\|^2 + \|H\|_2\|\boldsymbol{J}\|_2}}{2\|\boldsymbol{J}\|_2\|H\|_2}.$$

Since $\left\|H(k_p\boldsymbol{I}+\sqrt{k_p}K_d)\right\| < \sqrt{\left\|H(k_p\boldsymbol{I}+\sqrt{k_p}K_d)\right\|^2 + \|H\|_2\|\boldsymbol{J}\|_2}$ and $\rho \geq 0$, the lower-bound is redundant. Therefore, (9a) bounds the level ρ of the PI set (6) for input admissibilty. The bound (9b) can be derived by noting that

the polytope $\{\boldsymbol{\tau} : \pm h_j \boldsymbol{\tau} \leq 1, j = 1, \ldots, m\} = \bigcap \boldsymbol{P}_{j=1,\ldots,m}\{\boldsymbol{\tau} : \|h_j \boldsymbol{\tau}\| \leq 1\}$ is the intersection of degenerate ellipsoids $\{\boldsymbol{\tau} : \|h_j \boldsymbol{\tau}\| \leq 1\}$. □

Proposition 1 provides two methods for bounding the level ρ^2 of the PI set (6) depending on the nature of the torque constraint set $\mathcal{T}$. For non-CMG actuators, the torque constraint set will typically be polyhedral. For instance, if each of the actuator command u_i has a lower $\underline{\boldsymbol{u}}_i$ and upper $\bar{u_i}$ bound on its authority $\underline{\boldsymbol{u}}_i \leq u_i \leq \bar{\boldsymbol{u}}_i$ then the input constraint set will be a box $\mathcal{U} = \{\boldsymbol{u} : \underline{\boldsymbol{u}}_i \leq u_i \leq \bar{\boldsymbol{u}}_i\}$ and the torque constraint set $\mathcal{T} = \boldsymbol{T}\mathcal{U}$ will be a polyhedron (specifically a zonotope) [49].

For CMGs, the torque constraint set $\mathcal{T} = \boldsymbol{T}(\delta)\mathcal{U}$ is time-varying since the matrix $\boldsymbol{T}(\delta)$ depends on the gimbal angles $\delta(t)$. For the triplet steering-law, we can inner-approximated the angular momentum envelop of the CMG array as the Cartesian product of circles [37]. Thus, we can inner-approximate $\bar{\mathcal{T}} \subseteq \mathcal{T}(\delta)$ the torque constraint set $\mathcal{T}$ using a time-invariant ellipsoidal set $\bar{\mathcal{T}}$. More generally, we can use the matrix $H = \underline{\sigma}\boldsymbol{I}$ for the ellipsoidal-bound where $\underline{\sigma} \leq \|\boldsymbol{T}(\delta)\|_2$ is the lower-bound on the spectral-norm of the matrix $\boldsymbol{T}(\delta)$ for a particular steering law. This is necessary so that the level bound $\rho^2 \in (0, 2)$ does not depend on the state $\delta(t)$ of the CMG-array, which is unknown to the ISMP.

B. Search Graph

In this section, we describe the generation of the nodes $\mathbb{I}$ and edges $\mathbb{E}$ of the search graph $\mathbb{G} = (\mathbb{I}, \mathbb{E})$ used by the ISMP.

1. Search Graph Nodes

The nodes $i \in \mathbb{I}$ of the search graph $\mathbb{G} = (\mathbb{I}, \mathbb{E})$ index the reference orientations $\boldsymbol{r}_i \in \bar{\mathbb{H}}$ and the corresponding PI set $\mathcal{O}_i$ such that $(\boldsymbol{r}_i, 0) \in \mathcal{O}_i$. For some attitude motion planning problem, it is necessary to keep the spacecraft orientation in a constant keep-in cone $\mathcal{Q}$. For instance, our experimental platform has a crucial keep-in constraint to prevent damage, see Section IV.A. In practice, a constant keep-in constraints can arise from a spacecraft needing to keep its solar panels pointed at the sun. Since we are memory-constrained, we would like to ensure that we only sample reference quaternions $\boldsymbol{r}_i \in \bar{\mathbb{H}}$ for our search-graph $\mathbb{G}$ that satisfy the keep-in cone constraints $\boldsymbol{r}_i \in \mathcal{Q}$. The following proposition provides a parameterization of quaterions that satisfy the keep-in cone constraints.

Proposition 2 *The keep-in cone* (5) *can be written as*

$$\mathcal{Q} = \left\{ \boldsymbol{q} = \boldsymbol{P}_+ \boldsymbol{q}_+ + \boldsymbol{P}_- \boldsymbol{q}_- : \boldsymbol{q}_- \in \sin\frac{\alpha}{2}\mathbb{B}^2, \boldsymbol{q}_+ \in \sqrt{1 - \|\boldsymbol{q}_-\|^2}\mathbb{S}^1 \right\} \tag{10}$$

where $\boldsymbol{P}_+$ and $\boldsymbol{P}_-$ were defined in (8) *and, $\mathbb{B}^2 \subset \mathbb{R}^2$ and $\mathbb{S}^1$ are the unit-disk and unit-circle in $\mathbb{R}^2$, respectively.*

Proof: Let $\mathcal{Q}$ denote the original keep-in cone (5) and $\mathcal{Q}'$ denote our alternative parameterization (10). We will prove $\mathcal{Q} = \mathcal{Q}'$.

Using the Euler-Rodrigues formula $\boldsymbol{R}(\boldsymbol{q}) = \boldsymbol{I} + 2\boldsymbol{q}_0\boldsymbol{q}_v^\times + 2\boldsymbol{q}_v^\times\boldsymbol{q}_v^\times$, the keep-in cone (5) can be written in the form $\mathcal{Q} = \left\{\boldsymbol{q} : \boldsymbol{q}^\top\boldsymbol{P}\boldsymbol{q} \geq \cos\alpha\right\}$ where $\boldsymbol{P}$ is given by (4). Consider $\boldsymbol{q} = \boldsymbol{P}_+\boldsymbol{q}_+ + \boldsymbol{P}_-\boldsymbol{q}_- \in \mathcal{Q}'$. Then, $\boldsymbol{q}^\top\boldsymbol{P}\boldsymbol{q} = \|\boldsymbol{q}_+\|^2 - \|\boldsymbol{q}_-\|^2$ since the columns of $\boldsymbol{P}_+ \in \mathbb{R}^{4\times 2}$ and $\boldsymbol{P}_- \in \mathbb{R}^{4\times 2}$ are respectively the eigenvectors corresponding to the repeated eigenvalues $\lambda_+ = 1$ and $\lambda_- = -1$ of $\boldsymbol{P}$ [32]. Since $\boldsymbol{q}_+ \in \sqrt{1 - \|\boldsymbol{q}_-\|^2}\mathbb{S}^1$, we have $\|\boldsymbol{q}_+\|^2 = 1 - \|\boldsymbol{q}_-\|^2$. Thus, $\boldsymbol{q}^\top\boldsymbol{P}\boldsymbol{q} = 1 - 2\|\boldsymbol{q}_-\|^2$. For $\boldsymbol{q}_- \in \sin\frac{\alpha}{2}\mathbb{B}^2$, we have

$$\boldsymbol{q}^\top\boldsymbol{P}\boldsymbol{q} = 1 - 2\|\boldsymbol{q}_-\|^2 \geq 1 - 2\sin\left(\tfrac{\alpha}{2}\right)^2 = \cos\alpha$$

where $\sin(\alpha/2)^2 = \frac{1}{2} - \frac{1}{2}\cos\alpha$. Thus, $\boldsymbol{q} \in \mathcal{Q}$ and therefore, $\mathcal{Q}' \subseteq \mathcal{Q}$.

Now consider $\boldsymbol{q} \notin \mathcal{Q}'$. Then, either $\boldsymbol{q}_+ \notin \sqrt{1 - \|\boldsymbol{q}_-\|^2}\mathbb{S}^1$ or $\boldsymbol{q}_- \notin \sin\frac{\alpha}{2}\mathbb{B}^2$. If $\boldsymbol{q}_+ \notin \sqrt{1 - \|\boldsymbol{q}_-\|^2}\mathbb{S}^1$ then $\|\boldsymbol{q}\|^2 = \|\boldsymbol{P}_+\boldsymbol{q}_+ + \boldsymbol{P}_-\boldsymbol{q}_-\|^2 = \|\boldsymbol{q}_+\|^2 + \|\boldsymbol{q}_-\|^2 \neq 1$. Thus, $\boldsymbol{q} \notin \bar{\mathbb{H}} \supseteq \mathcal{Q}$. Conversely, if $\boldsymbol{q}_- \notin \sin\frac{\alpha}{2}\mathbb{B}^2$ then $\boldsymbol{q}^\top\boldsymbol{P}\boldsymbol{q} < 1 - 2\sin\left(\frac{\alpha}{2}\right)^2 = \cos\alpha$. Thus, $\boldsymbol{q} \notin \mathcal{Q}$. Therefore, $\mathcal{Q} \subseteq \mathcal{Q}'$ and hence $\mathcal{Q} = \mathcal{Q}'$. □

The orthogonal matrix $\boldsymbol{P}_+ \in \mathbb{R}^{4\times 2}$ parameterizes the manifold of quaternions $\boldsymbol{P}_+\boldsymbol{q}_+ \in \bar{\mathbb{H}}$ that rotates the body-frame vector $\boldsymbol{b}$ about the inertia-frame vector $\boldsymbol{d}$. These rotations $\boldsymbol{P}_+\boldsymbol{q}_+ \in \bar{\mathbb{H}}$ will not change the alignment of these vectors i.e. $\boldsymbol{d}^\top\boldsymbol{R}(\boldsymbol{P}_+\boldsymbol{q}_+)\boldsymbol{b}$ is constant for all $\boldsymbol{q}_+ \in \mathbb{S}^1$. According to Proposition 2, we can freely-sample these rotations by sampling the unit-circle $q_+ \in \sqrt{1 - \|q_-\|^2}\mathbb{S}^1 \subset \mathbb{R}^2$ and lifting into quaternions $P_+q_+ \in \bar{\mathbb{H}} \subset \mathbb{R}^4$. The scaling $\sqrt{1 - \|q_-\|^2}$ ensures that the sum $\boldsymbol{P}_+\boldsymbol{q}_+ + \boldsymbol{P}_-\boldsymbol{q}_-$ is a unit-quaternion i.e. $\|\boldsymbol{q}_+\| = \sqrt{1 - \|\boldsymbol{q}_-\|^2}$ where $\|\boldsymbol{P}_+\boldsymbol{q}_+\| = \|\boldsymbol{q}_+\|$ since $\boldsymbol{P}_+$ is orthogonal. In contrast, the orthogonal matrix $\boldsymbol{P}_- \in \mathbb{R}^{4\times 2}$ parameterizes the two-dimensional manifold of quaternions $\boldsymbol{P}_-\boldsymbol{q}_-$ that changes the alignment $\boldsymbol{d}^\top\boldsymbol{R}(\boldsymbol{P}_-\boldsymbol{q}_-)\boldsymbol{b}$. According to Proposition 2, we must limit the magnitude $\|\boldsymbol{q}_-\| \leq \sin\frac{\alpha}{2}$ of quaternions in this subspace to prevent the vectors $\boldsymbol{d}$ and $\boldsymbol{b}$ from aligning $\boldsymbol{d}^\top\boldsymbol{R}(\boldsymbol{P}_-\boldsymbol{q}_-)\boldsymbol{b} \geq \cos\alpha$. According to Proposition 2, sufficiently small rotations can be obtained by sampling the disk $q_+ \in \sin\frac{\alpha}{2}\mathbb{B}^2 \subset \mathbb{R}^2$ and lifting into the quaternions $P_-q_- \in \bar{\mathbb{H}} \subset \mathbb{R}^4$.

According to Proposition 2, we can sample safe reference quaternions $\boldsymbol{r} = \boldsymbol{P}_+\boldsymbol{r}_+ + \boldsymbol{P}_-\boldsymbol{r}_- \in \mathcal{Q}$ by sampling the disk $\boldsymbol{r}_+ \in \sin(\alpha/2)\mathbb{B}^2$ and the circle $\boldsymbol{r}_+ \in \sqrt{1 - \|\boldsymbol{r}_-\|^2}\mathbb{S}^1$. Thus, to create a grid of reference quaternions $\boldsymbol{r}_i \in \mathcal{Q}$, we need to grid the planar disk $\sin(\alpha/2)\mathbb{B}^2 \subset \mathbb{R}^2$ and planar circle $\sin(\alpha/2)\mathbb{B}^2 \subset \mathbb{R}^2$. The naive method for gridding the planar disk $\sin(\alpha/2)\mathbb{B}^2 \subset \mathbb{R}^2$ is to uniformly grid its polar coordinates i.e. radius and angle. However, this creates a non-uniform grid $\boldsymbol{r}_{-,i}$ that is dense near the origin and sparse near the boundary of the disk. Instead, we will grid the disk using the process demonstrated by Fig. 1. First, we inscribe the planar disk $\sin(\alpha/2)\mathbb{B}^2 \subset \mathbb{R}^2$ by a regular n-sided polygon. The regular n-sided polygon is then divided into n triangles. These triangles can then be sub-divided into a triangular mesh to produce a uniform gird on the planar disk. Each of the grid points shown Fig. 1 represents a sampling of $\boldsymbol{r}_- \in \sin(\alpha/2)\mathbb{B}^2 \subset \mathbb{R}^2$. Gridding the $\sqrt{1 - \|\boldsymbol{r}_-\|^2}\mathbb{S}^1 \subset \mathbb{R}^2$ to sample $\boldsymbol{r}_+ \in \mathbb{R}^2$ is straightforward since we can uniformly grid the angles $[0, 2\pi)$ to produce uniformly distributed samples $\boldsymbol{r}_{+,i}$. The reference quaternions are then given by $\boldsymbol{r}_i = \boldsymbol{P}_+\boldsymbol{r}_{+,i} + \boldsymbol{P}_-\boldsymbol{r}_{-,i} \in \bar{\mathbb{H}}$ according to Proposition 2. Although this parameterization does not provide a uniform gridding of the keep-in cone, it can be easily modified for this purpose [52].

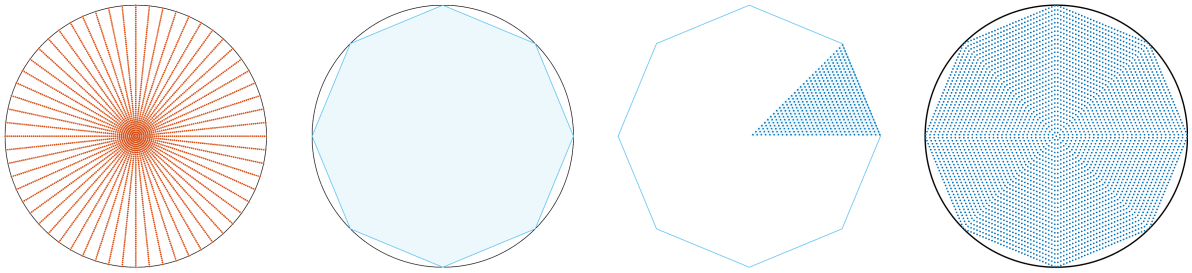

(a) (b) (c) (d)

Fig. 1 (a) Non-uniform grid produced by gridding the polar coordinates. (b) Inscription of the planar disk by a octagon. (c) Triangular mesh on a triangular slice of the octagon. (d) Resulting uniform mesh.

The same search-graph $\mathbb{G} = (\mathbb{I}, \mathbb{E})$ will be used for each of our experiments where the references $\boldsymbol{r}_i$ for $i \in \mathbb{I}$ were generated using the procedure above. The keep-in cone (5) requires that the spacecraft z-axis $\boldsymbol{b} = (0, 0, 1)$ should be aligned with the inertial z-axis $\boldsymbol{d}_Q = (0, 0, 1)$ within an angle of $\alpha_Q = 20^\circ$. We inscribed the planar disk $\sin(10^\circ)\mathbb{B}^2 \subset \mathbb{R}^2$ by a 8-sided octagon shown in Fig. 1(b). For each of the 8 resulting triangles, we produce a uniform triangular mesh with 496 vertices. This produced a uniform sampling for $\boldsymbol{r}_{-,i} \in \mathbb{R}^2$. For the keep-in cone parameters $\boldsymbol{b} = (0, 0, 1)$ and $\boldsymbol{d}_Q = (0, 0, 1)$, the eigenvector matrix $\boldsymbol{P}_-$ in (8) maps the grid-points $\boldsymbol{r}_{-,i}$ to quaternions $\boldsymbol{r} = \boldsymbol{P}_+\boldsymbol{r}_{+,i} + \boldsymbol{P}_-\boldsymbol{r}_{-,i} \in \bar{\mathbb{H}}$ representing rotations about the x-axis and y-axis of the spacecraft. The grid-points $\boldsymbol{r}_{+,i} \in \sqrt{1 - \|\boldsymbol{r}_-\|^2}\mathbb{S}^1$ will be mapped by $\boldsymbol{P}_+$ in (8) to quaternions representing rotations about the z-axis of the spacecraft. Since our experiments did not require large rotations about the z-axis, we uniformly gridded a 10° arc of the circle $\sqrt{1 - \|\boldsymbol{r}_-\|^2}\mathbb{S}^1$ with 1° increments, rather than the entire circle.

2. Search Graph Edges

The edges $(i, j) \in \mathbb{E}$ of the graph $\mathbb{G} = (\mathbb{I}, \mathbb{E})$ indicate that the state $\boldsymbol{x}(t) = (\boldsymbol{q}(t), \boldsymbol{\omega}(t))$ of the spacecraft dynamics (1) will enter the safe set $\mathcal{O}_j$ while tracking the i-th reference $\boldsymbol{r}_i \in \bar{\mathbb{H}}$ without leaving the current safe set $\mathcal{O}_i$ (see Line 5 of Algorithm 1). This will occur if the equilibrium state $(\boldsymbol{r}_i, 0) \in \bar{\mathbb{H}} \times \mathbb{R}^3$ is contained $(\boldsymbol{r}_i, 0) \in \text{int}(\mathcal{O}_j)$ in the interior $\text{int}(\mathcal{O}_j)$ of the j-th PI set $\mathcal{O}_j$. This can be efficiently checked using the expression

$$|\boldsymbol{r}_i^\top \boldsymbol{r}_j| > 1 - \tfrac{1}{2}\rho_i^2 \tag{11}$$

for $i, j \in \mathbb{I}$. This condition follows directly from substituting $\boldsymbol{q} = \boldsymbol{r}_j$ and $\boldsymbol{\omega} = 0$ into the Lyapunov function (2). According to (6), increasing the level $\rho_i^2 \in (0, 2)$ will produce a larger PI set $\mathcal{O}_i$, increasing the connectivity (5) of the graph, but also increasing the chance of collision $\boldsymbol{C}\mathcal{O}_i \cap \mathcal{K}_k \neq \varnothing$ with an obstacle $\mathcal{K}_k$.

Note that in general the graph $\mathbb{G} = (\mathbb{I}, \mathbb{E})$ has directed edges since the levels are not necessarily identical $\rho_i \neq \rho_j$ i.e. $(\boldsymbol{r}_i, 0) \in \text{int}(\mathcal{O}_j) \nRightarrow (\boldsymbol{r}_j, 0) \in \text{int}(\mathcal{O}_i)$. For the search-graph $\mathbb{G} = (\mathbb{I}, \mathbb{E})$ used in the experiments we used a uniform level

$\rho_i^2 = 2 - 2\cos(2^\circ)$ for all PI sets (6). The search-graph used in the experiments has 3,930 nodes and 416,660 edges requiring 6.69 megabytes to store.

IV. Experimental Results

In this section, we present experimental result demonstrating the ISMP for spacecraft attitude motion planning.

A. Experimental Setup and Methodology

Experimental evaluation of the ISMP was conducted using the Air Force Research Laboratory (AFRL) Space Vehicles Directorate's large spherical air-bearing spacecraft simulator, ReBEL (Resilient Bus Experimental Laboratory). AFRL has operated such spacecraft simulators since the 1980s to investigate a wide range of topics including fault detection and isolation algorithms and robust nonlinear controls [37, 38]. The ReBEL platform uses AFRL heritage hardware from the Advanced Structural Technology Research Experiment (ASTREX) [53], one of AFRL's first spacecraft emulators. ReBEL uses ASTREX's 18.9-in-diameter spherical air bearing which is capable of supporting loads of up to 15,000 lbs [38]. ReBEL provides approximately ±35 degrees of motion about the horizontal axes and unconstrained rotation about its vertical axis. For the safety of the experimental platform, we enforce a tighter $20^\circ < 35^\circ$ keep-in cone constraint since over-rotation can cause the support structure to collide with the air bearing which could damage the platform see Figure 2. The moment-of-inerta J of the platform can be estimated using standard methods from literature [54].

Fig. 2 AFRL ReBEL Spacecraft Simulator

The experiments used existing systems on the ReBEL testbed without the need for specialized hardware or software.

The ReBEL testbed uses an array of 6 CMGs in a rooftop configuration for attitude actuation. A 6-CMG roof array configuration contains no elliptic internal singularities and are, therefore, able to achieve a non-singular solution internal to the angular momentum space at every point by leveraging intelligent steering laws [37]. The platform makes use of a Moore-Penrose Inverse steering law for allocating actuator commands to achieve the desired torque; however, the triplet steering-law can be used to ensure no singularities can occur. For this experiment, the desired torque was specified by the quaternion controller (1c). The orientation and angular velocity of the platform are directly measured using a motion capture system and inertial measurement unit, respectively. The ReBEL platform has software to fuse and smooth the raw sensor measurements.

Three experimental scenarios were setup and conducted to test the ISMP on the attitude spacecraft simulator.

B. Illustrative Scenario 1: Stopping

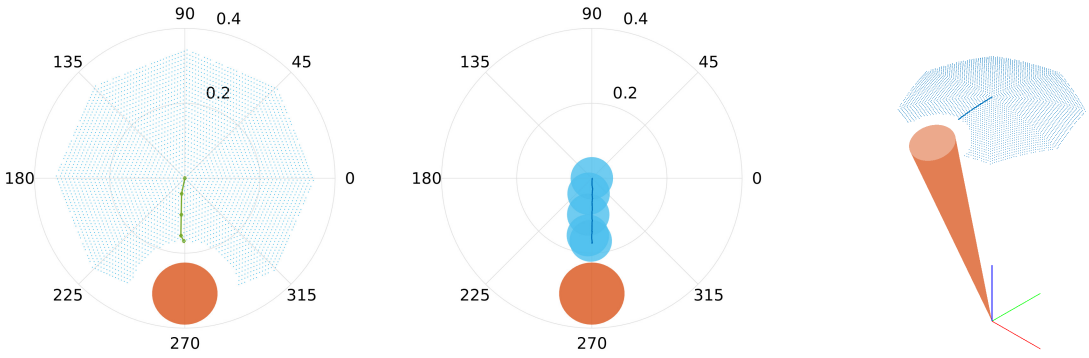

(a) (b) (c)

Fig. 3 The planned (a) and actual (b) paths of the z-axis of the spacecraft during the stopping scenario. This scenario shows that the ISMP can ensure constraint satisfaction despite overshoot. (c) The planned and actual path of the z-axis is shown in three-dimensions.

In this experimental scenario, the spacecraft must perform a re-orientation maneuver that causes it to move towards a keep-out cone $\mathcal{K}$ as shown in Fig. 3(a). The ISMP must manage the momentum of the spacecraft to prevent it from overshooting into the keep-out cone. The spacecraft starts from the equilibrium state $\boldsymbol{x}(0) = (\boldsymbol{q}(0), \boldsymbol{\omega}(0))$ where it is initial stationary $\boldsymbol{\omega}(0) = 0$ and in the home-orientation $\boldsymbol{q}(0) = \mathbb{1}$. The target orientation is a 10° rotation about the x-axis $\boldsymbol{r}_\infty = (\cos 5°, 0, \sin 5°, 0) \in \bar{\mathbb{H}}$. During the maneuver, the z-axis $\boldsymbol{b} = (0, 0, 1)$ of the spacecraft must be kept out of a single keep-out cone $\mathcal{K}$ with cone angle $\alpha = 5°$ inertia-frame axis $\boldsymbol{d} = (0, -0.2024, 0.9563)$. The inertial-axis $\boldsymbol{d}$ corresponds to rotating the inertia z-axis $(0, 0, 1)$ about the x-axis by 17°. Thus, a 2° overshoot will cause the spacecraft to enter the keep-out cone. This is a plausible threat due to the high-inertia of the spacecraft emulator. The experimental scenario is shown in Fig. 3(a) with the planning graph described in Section III.B. For clarity of the plots, the body-frame

axis $\boldsymbol{b} = (0, 0, 1)$ will always be the z-axis of the spacecraft, but in practice this can be any vector.

Theorem 1 was applied $3,930$ times to check whether each of the $|\mathbb{I}| = 3,930$ PI sets $\mathcal{O}_i$ collides $\boldsymbol{C}\mathcal{O}_i \cap \mathcal{K}_1 \neq \varnothing$ with the single obstacles $\mathcal{K}_1$. Performing these collision checks required 0.525 milliseconds on a 2019 MacBook Pro with a 2.6 GHz 6-Core Intel Core i7 process and 16GB of RAM. After removing the unsafe nodes, the reduced search-graph shown in Fig. 3(a) has $3,535$ nodes and $370,687$ edges. This reduced search-graph was searched using Dijkstra shortest-path algorithm implemented in MATLAB's `shortestpath` function. The graph search required 9.4 milliseconds to produced a sequence $\{\boldsymbol{r}_{\sigma_k}\}_{k=1}^{8} \subset \mathbb{I}$ of 8 references $\boldsymbol{r}_{\sigma_k} \in \bar{\mathbb{H}}$ that safely guides the spacecraft from the initial state $\boldsymbol{x}_0 = (\boldsymbol{q}_0, 0) \in \bar{\mathbb{H}} \times \mathbb{R}^3$ to the target equilibrium state $\boldsymbol{x}_\infty = (\boldsymbol{r}_\infty, 0) \in \bar{\mathbb{H}} \times \mathbb{R}^3$. The planned path for the z-axis of the spacecraft is shown in Fig. 3(a).

Following Algorithm 1, the reference $\boldsymbol{r}_{\sigma_k}$ tracked by the controller (1c) is updated $k \leftarrow k + 1$ each time the spacecraft (1) state $\boldsymbol{x}(t) = (\boldsymbol{q}(t), \omega(t) \in \bar{\mathbb{H}} \times \mathbb{R}^3$ enters the next PI set $\mathcal{O}_{\sigma_{k+1}} \subseteq \bar{\mathbb{H}} \times \mathbb{R}^3$. The resulting trajectory traced by the z-axis of the spacecraft is shown in Fig. 3(b). Note that the actual trajectory $z(t)$ of the z-axis of the spacecraft does not perfectly track the planned path $z \otimes \boldsymbol{r}_i$. However, the ISMP avoids the keep-out cone $\mathcal{K}$ since the trajectory remains inside $z(t) \in \mathcal{O}_{\sigma_k}$ the corridor $\{\mathcal{O}_{\sigma_k}\}_{k=1}^{8} \subset \mathbb{I}$ of CAPI sets.

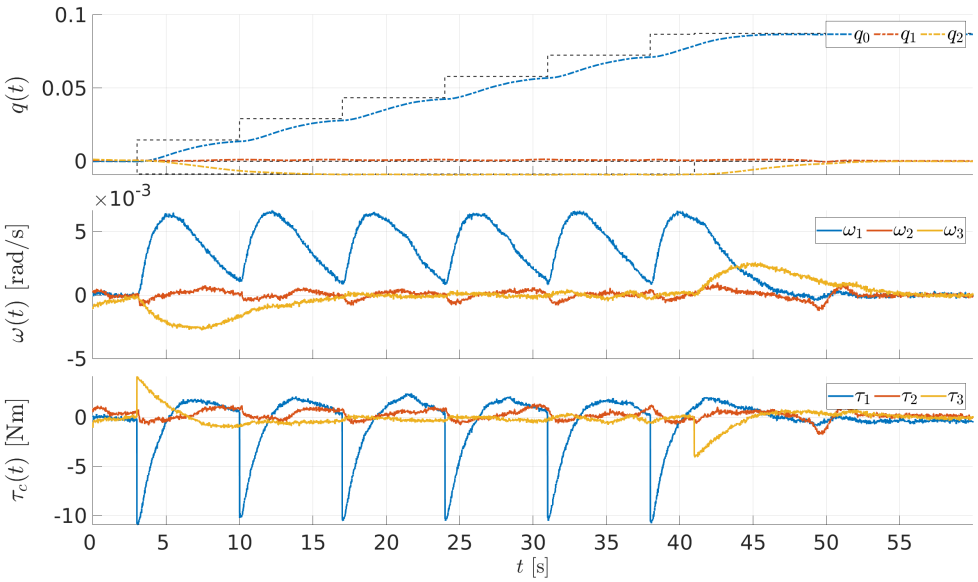

Fig. 4 State $(\boldsymbol{q}(t), \omega(t))$ and torque $\tau(t)$ trajectories for the spacecraft in the stopping experimental scenario.

Fig. 4 shows the state and input trajectories of the spacecraft versus time. Fig. 4 shows the vector-part of the quaternion $\boldsymbol{q}_v(t)$, angular velocity $\boldsymbol{\omega}(t)$, and torque $\boldsymbol{\tau}(t)$, respectively. Since the spacecraft maneuvers are relatively small $< 20°$, we only show the vector-part $\boldsymbol{q}_v(t)$ of the quaternion since $\boldsymbol{q}_0(t) \approx 1$. The ISMP plans a series of small intermediate set-point changes that eliminate overshoot and therefore prevent the spacecraft state from leaving the PI sets $\mathcal{O}_{\sigma_k}$. This demonstrates the main advantage of the ISMP. Since the spacecraft dynamics are incorporated into the

planning process through the use of PI sets, we can prevent the momentum of the high-inertia spacecraft from carrying it into a keep-out cone.

C. Illustrative Scenario 2: Slalom

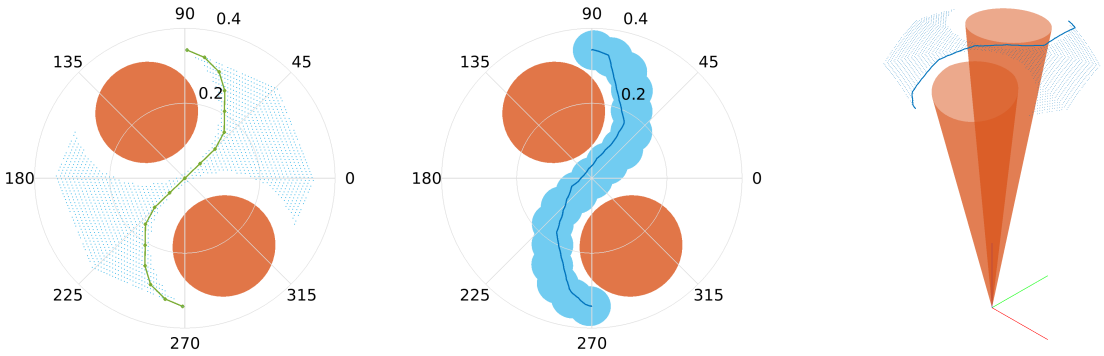

(a) (b) (c)

Fig. 5 The planned (a) and actual (b) paths of the z-axis of the spacecraft during the slalom scenario. This scenario shows that the ISMP can ensure that the spacecraft momentum is reversed to avoid the second keep-out cone. (c) The planned and actual path of the z-axis is shown in three-dimensions.

In this experimental scenario, the spacecraft must perform a slalom maneuver to avoid a pair of keep-out cones $\mathcal{K}_{1,2}$, as shown in Fig. 5(a). This maneuver is analogous to a slalom (or double-lane-change) maneuver, which is a standard experimental test for evaluating the handling of a car. This test scenario will require the ISMP to reverse the momentum of the spacecraft to transition from avoiding the first keep-out cone to the second. The spacecraft starts from the equilibrium state $\boldsymbol{x}(0) = (\boldsymbol{q}(0), \boldsymbol{\omega}(0))$ where it is initial stationary $\boldsymbol{\omega}(0) = 0$ and rotated -20° about the x-axis $\boldsymbol{r}_0 = (\cos 10^\circ, 0, -\sin 10^\circ, 0) \in \bar{\mathbb{H}}$. The target orientation is a $+20^\circ$ rotation about the x-axis $\boldsymbol{r}_\infty = (\cos 10^\circ, 0, \sin 10^\circ, 0) \in \bar{\mathbb{H}}$. Thus, the spacecraft will slew 40° total.

During the maneuver, the z-axis $\boldsymbol{b}_{1,2} = (0, 0, 1)$ of the spacecraft must be kept out of two keep-out cones $\mathcal{K}_{1,2}$. For the first keep-out cone, the inertia-frame vector is $\boldsymbol{d}_1 = (0.1040, -0.1801, 0.9781)$. This corresponds to rotating the inertia z-axis $(0, 0, 1)$, $+12^\circ$ about the inertia x-axis $(1, 0, 0)$ and then 30° about the inertia z-axis $(0, 0, 1)$. The second keep-out cone has the inertia-frame vector is $\boldsymbol{d}_2 = (-0.1040, 0.1801, 0.9781)$. This corresponds to rotating the inertia z-axis $(0, 0, 1)$, -12° about the inertia x-axis $(1, 0, 0)$ and then 30° about the inertia z-axis $(0, 0, 1)$. Both keep-out cones have an angle of 8°. The experimental scenario is shown in Fig. 5(a) with the planing graph described in Section III.B.

Theorem 1 was applied $7,860$ times to check for collisions $\boldsymbol{CO}_i \cap \mathcal{K}_1 \neq \varnothing$ between the $|\mathbb{I}| = 3,930$ PI sets $\boldsymbol{O}_i$ and the 2 the keep-out cones $\mathcal{K}_{1,2}$. Performing these collision checks required a total of 1.022 milliseconds. After removing unsafe nodes, the reduced search-graph shown in Fig. 3(a) has $1,644$ nodes and $146,842$ edges. This reduced

search-graph was searched using Dijkstra shortest-path algorithm requiring 20.0 milliseconds and producing a sequence $\{\boldsymbol{r}_{\sigma_k}\}_{k=1}^{29} \subset \mathbb{I}$ of 29 references $\boldsymbol{r}_{\sigma_k} \in \bar{\mathbb{H}}$ that safely guides the spacecraft from the initial state $\boldsymbol{x}_0 = (\boldsymbol{q}_0, 0) \in \bar{\mathbb{H}} \times \mathbb{R}^3$ to the target equilibrium state $\boldsymbol{x}_\infty = (\boldsymbol{r}_\infty, 0) \in \bar{\mathbb{H}} \times \mathbb{R}^3$.

Following Algorithm 1, the reference $\boldsymbol{r}_{\sigma_k}$ tracked by the controller (1c) is updated $k \leftarrow k+1$ each time the spacecraft (1) state $\boldsymbol{x}(t) = (\boldsymbol{q}(t), \boldsymbol{\omega}(t) \in \bar{\mathbb{H}} \times \mathbb{R}^3$ enters the next PI set $\mathcal{O}_{\sigma_{k+1}} \subseteq \bar{\mathbb{H}} \times \mathbb{R}^3$. Thus, the ISMP creates a reference trajectory $r(t) = \boldsymbol{r}_{\sigma_k}$ consisting of a sequence of steps. Since the reference $\boldsymbol{r}_{\sigma_k}$ is constantly updating, the system has transient tracking errors resulting in imperfect tracking of the planned path. However, the trajectory remained inside $z(t) \in \mathcal{O}_{\sigma_k}$ the corridor $\{\mathcal{O}_{\sigma_k}\}_{k=1}^{29}$ of CAPI sets despite transient tracking errors. Thus, the ISMP prevented the spacecraft from entering the keep-out cones $\mathcal{K}_{1,2}$.

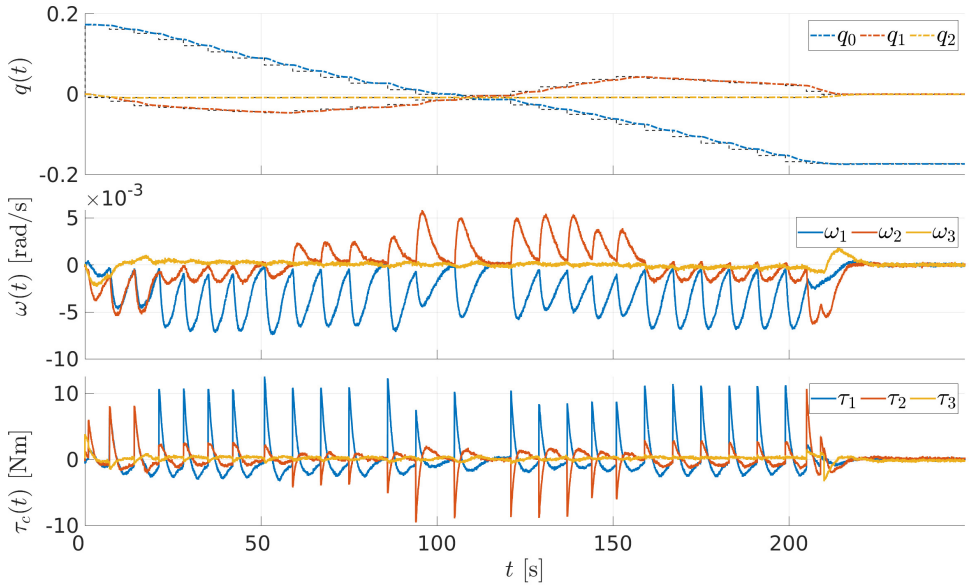

Fig. 6 State $(\boldsymbol{q}(t), \boldsymbol{\omega}(t))$ and torque $\boldsymbol{\tau}(t)$ trajectories for the spacecraft in the slalom experimental scenario.

Fig. 6 shows the state and input trajectories of the spacecraft versus time. Fig. 6 shows the vector-part of the quaternion $\boldsymbol{q}_v(t)$, angular velocity $\boldsymbol{\omega}(t)$, and torque $\boldsymbol{\tau}(t)$, respectively. Since the spacecraft maneuvers are relatively small $< 20°$, we only show the vector-part $\boldsymbol{q}_v(t)$ of the quaternion since $\boldsymbol{q}_0(t) \approx 1$. Although the initial $\boldsymbol{r}_0 = (\cos 10°, 0, -\sin 10°, 0) \in \bar{\mathbb{H}}$ and target $\boldsymbol{r}_\infty = (\cos 10°, 0, \sin 10°, 0) \in \bar{\mathbb{H}}$ orientations are only rotations about the x-axis, the ISMP rotates the spacecraft about the y-axis to avoid pointing the z-axis at the keep-out cones. First, the spacecraft need perform a negative rotation about y-axis and then a positive rotation. This is a difficult maneuver since the ISMP must impart a high angular momentum in one direction and then reverse before entering the second keep-out cone.

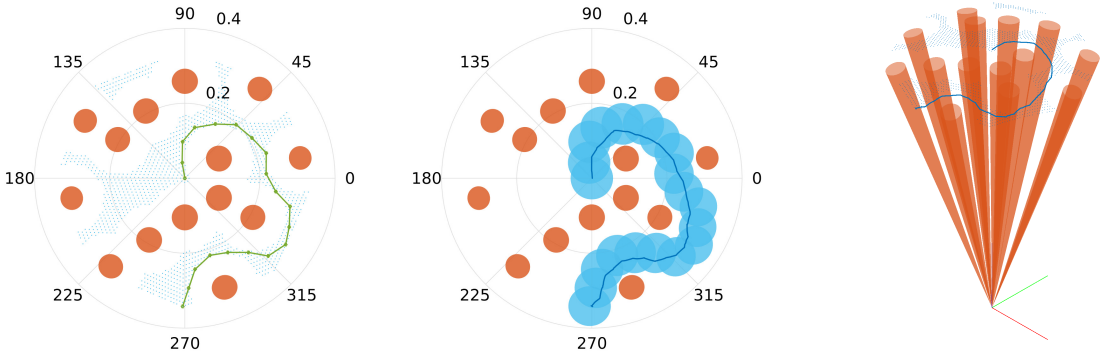

(a) (b) (c)

Fig. 7 The planned (a) and actual (b) paths of the z-axis of the spacecraft during the slalom scenario. This scenario shows that the ISMP can ensure that the spacecraft momentum is reversed to avoid the second keep-out cone. (c) The planned and actual path of the z-axis is shown in three-dimensions.

D. Challenging Scenario - Maze

In this experimental scenario, the spacecraft must escape from a 'maze' of keep-out cones. The objective of this experiment is to provide an unrealistically difficult scenario to stress-test the capabilities of the ISMP. The spacecraft starts from rest $\boldsymbol{\omega}(0) = 0$ at the home-position $\boldsymbol{q}_0 = \mathbb{1}$. The target orientation is a 20° rotation about the x-axis $\boldsymbol{r}_\infty = (\cos 10^\circ, 0, \sin 10^\circ, 0) \in \bar{\mathbb{H}}$. The z-axis of the spacecraft must avoid 14 keep-out cones randomly placed in the keep-in cone $\mathcal{Q}$ with keep-out angles $\alpha = 2^\circ$. Again, the body-frame axis $\boldsymbol{q} = (0, 0, 1)$ is the z-axis of the spacecraft in order to make our figures clearer. The experimental scenario is shown in Fig. 7(a) with the planing graph described in Section III.B.

Theorem 1 was applied $55,020$ times to check for collisions $\boldsymbol{CO}_i \cap \mathcal{K}_1 \neq \varnothing$ between the $|\mathbb{I}| = 3,930$ PI sets $\mathcal{O}_i$ and the 14 keep-out cones $\mathcal{K}$. Performing these collision checks required a total of 9.08 milliseconds. After removing unsafe nodes, the reduced search-graph shown in Fig. 3(a) has $1,132$ nodes and $70,942$ edges. This reduced search-graph was searched using Dijkstra shortest-path algorithm requiring 19.8 milliseconds and produced a sequence $\{\boldsymbol{r}_{\sigma_k}\}_{k=1}^{32} \subset \mathbb{I}$ of 32 references $\boldsymbol{r}_{\sigma_k} \in \bar{\mathbb{H}}$ that safely guides the spacecraft from the initial state $\boldsymbol{x}_0 = (\boldsymbol{q}_0, 0) \in \bar{\mathbb{H}} \times \mathbb{R}^3$ to the target equilibrium state $\boldsymbol{x}_\infty = (\boldsymbol{r}_\infty, 0) \in \bar{\mathbb{H}} \times \mathbb{R}^3$. The planned path for the z-axis of the spacecraft is shown in Fig. 7(a). The trajectory $z(t)$ traced by the z-axis of the spacecraft is shown in Fig. 7(b).

Again, the ISMP creates a reference trajectory $r(t) = \boldsymbol{r}_{\sigma_k}$ consisting of a sequence of steps resulting in imperfect tracking due to the transient tracking errors. However, the trajectory remained inside $z(t) \in \mathcal{O}_{\sigma_k}$ the corridor of CAPI sets $\{\mathcal{O}_{\sigma_k}\}_{i=1}^{29}$ despite tracking errors and therefore avoided the keep-out cones.

Fig. 8 shows the state and input trajectories of the spacecraft versus time. Fig. 8 shows the vector-part of the

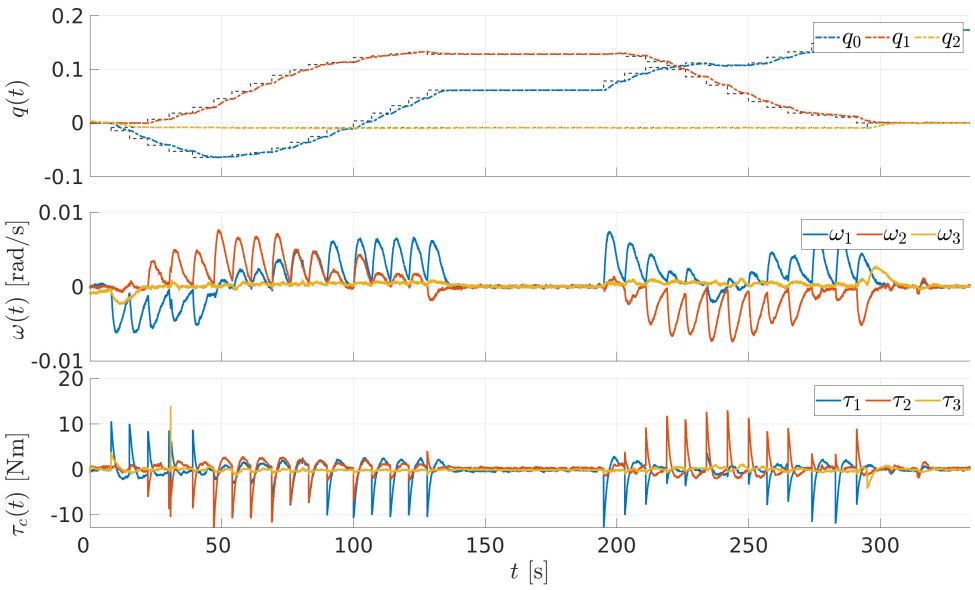

Fig. 8 Maze Scenario - Shows ISMP can deal complicated geometry

quaternion $\boldsymbol{q}_v(t)$, angular velocity $\boldsymbol{\omega}(t)$, and torque $\boldsymbol{\tau}(t)$, respectively. This scenario was challenging since the ISMP needed to constantly change orientation of the spacecraft to avoid the 14 of keep-out cones.

In this experimental scenario, the ISMP had difficulty switching between references $\boldsymbol{r}_{16}$ and $\boldsymbol{r}_{17}$. This was caused by a numerical issue we identified with the (literature [47, 48]) Lyapunov function (2) used by the ISMP to determine when to switch references. Switching references requires that the geodesic angle $\cos^{-1} e_0 = \cos^{-1} \boldsymbol{q}(t)^\top \boldsymbol{r}_{\sigma_{k+1}}$ between the actual $\boldsymbol{q}(t)$ and desired $\boldsymbol{r}_i$ orientations is sufficiently small $|\cos^{-1} e_0| \leq 2^\circ$. Alternatively, the Lyapunov function (2) evaluates the cosine of this condition i.e. $e_0 \geq \cos 2^\circ$. Although these conditions are theoretically equivalent, they are not numerically equivalent. The slope of the cosine-function is flat at the origin, which increases its susceptibility to noise. In particular, the ISMP only switches when $e_0 \approx 1$ to three digits of precision i.e. $e_0 \geq \cos 2^\circ = 0.9994$. In future work, we will rectify this numerical issue by deriving an novel Lyapunov function that certifies the stability of the closed-loop systems (1) while providing better numerical properties for the switching condition.

V. Conclusions

This paper experimentally validated the ISMP for the spacecraft constrained attitude motion planning problem. We demonstrated that we can guide the attitude of a spacecraft from an initial state $\boldsymbol{x}(0) = (\boldsymbol{q}(0), \boldsymbol{\omega}(0))$ to a desired equilibrium $\boldsymbol{x}_\infty = (\boldsymbol{r}_\infty, 0)$ while avoiding keep-out cones and respecting other constraints on the states and inputs of the spacecraft. We described PI sets (6) for the closed-loop spacecraft dynamics (1). We presented methods for ensure that these PI sets $\mathcal{O}$ are safe (output admissible) and satisfy angular velocity and torque constraints. We described a method for gridding reference quaternions from a keep-in cone. Finally, we presented experimental results that validate the

ISMP for spacecraft attitude motion planning. These experimental results show that by incorporating the spacecraft dynamics into the motion planning process, the ISMP can manage the high-inertia of the spacecraft to avoid collisions with keep-out cones.

VI. Funding

This material is based upon work supported by the National Science Foundation under NSF Grant Number CMMI-2105631 and the Air Force Office of Scientific Research under award number FA9550-22-1-0093. Any opinions, findings, and conclusions or recommendations expressed in this material are those of the authors and do not necessarily reflect the views of the National Science Foundation nor the United States Air Force.

References

[1] Kim, Y., Mesbahi, M., Singh, G., and Hadaegh, F., "On the constrained attitude control problem," *AIAA Guidance, Navigation, and Control Conference and Exhibit*, 2004, p. 5129.

[2] Hu, Q., Chi, B., and Akella, M., "Anti-Unwinding Attitude Control f Spacecraft with Forbidden Pointing Constraints," *J. of Guidance, Control, and Dynamics*, Vol. 42, No. 4, 2018.

[3] Shen, Q., Yue, C., Goh, C. H., Wu, B., and Wang, D., "Rigid-body attitude stabilization with attitude and angular rate constraints," *Automatica*, Vol. 90, 2018, pp. 157–163.

[4] Guo, Y., Li, C., and Ma, G., "Spacecraft autonomous attitude maneuver control by potential function method," *Acta Aeronautica et Astronautica Sinica*, Vol. 32, No. 3, 2011, pp. 457–464.

[5] Mengali, G., and Quarta, A. A., "Spacecraft control with constrained fast reorientation and accurate pointing," *The Aeronautical Journal*, Vol. 108, No. 1080, 2004, pp. 85–91.

[6] Lee, U., and Mesbahi, M., "Feedback control for spacecraft reorientation under attitude constraints via convex potentials," *IEEE Transactions on Aerospace and Electronic Systems*, Vol. 50, No. 4, 2014, pp. 2578–2592.

[7] Mclnnes, C. R., "Large angle slew maneuvers with autonomous sun vector avoidance," *Journal of Guidance, Control, and Dynamics*, Vol. 17, No. 4, 1994, pp. 875–877. https://doi.org/10.2514/3.21283, URL https://doi.org/10.2514/3.21283.

[8] Diaz Ramos, M., and Schaub, H., "Kinematic Steering Law for Conically Constrained Torque-Limited Spacecraft Attitude Control," *Journal of Guidance, Control, and Dynamics*, Vol. 41, No. 9, 2018, pp. 1990–2001. https://doi.org/10.2514/1.G002873, URL https://doi.org/10.2514/1.G002873.

[9] Lee, D. Y., Gupta, R., Kalabić, U. V., Di Cairano, S., Bloch, A. M., Cutler, J. W., and Kolmanovsky, I. V., "Geometric mechanics based nonlinear model predictive spacecraft attitude control with reaction wheels," *Journal of Guidance, Control, and Dynamics*, Vol. 40, No. 2, 2017, pp. 309–319.

[10] Walsh, A., and Forbes, J. R., "Constrained attitude control on SO (3) via semidefinite programming," *Journal of Guidance, Control, and Dynamics*, Vol. 41, No. 11, 2018, pp. 2483–2488.

[11] Sun, C., and Dai, R., "Spacecraft attitude control under constrained zones via quadratically constrained quadratic programming," *AIAA guidance, navigation, and control conference*, 2015, p. 2010.

[12] Nicotra, M. M., Liao-McPherson, D., Burlion, L., and Kolmanovsky, I. V., "Spacecraft Attitude Control With Nonconvex Constraints: An Explicit Reference Governor Approach," *IEEE Transactions on Automatic Control*, Vol. 65, No. 8, 2020, pp. 3677–3684. https://doi.org/10.1109/TAC.2019.2951303.

[13] Kim, Y., and Mesbahi, M., "Quadratically constrained attitude control via semidefinite programming," *IEEE Transactions on Automatic Control*, Vol. 49, No. 5, 2004, pp. 731–735.

[14] Melton, R. G., "Hybrid methods for determining time-optimal, constrained spacecraft reorientation maneuvers," *Acta Astronautica*, Vol. 94, No. 1, 2014, pp. 294–301. https://doi.org/https://doi.org/10.1016/j.actaastro.2013.05.007, URL https://www.sciencedirect.com/science/article/pii/S0094576513001574.

[15] Spiller, D., Ansalone, L., and Curti, F., "Particle Swarm Optimization for Time-Optimal Spacecraft Reorientation with Keep-Out Cones," *Journal of Guidance, Control, and Dynamics*, Vol. 39, No. 2, 2016, pp. 312–325. https://doi.org/10.2514/1.G001228, URL https://doi.org/10.2514/1.G001228.

[16] Kjellberg, H. C., and Lightsey, E. G., "Discretized quaternion constrained attitude pathfinding," *Journal of Guidance, Control, and Dynamics*, Vol. 39, No. 3, 2016, pp. 713–718.

[17] Weiss, A., Leve, F., Baldwin, M., Forbes, J. R., and Kolmanovsky, I., "Spacecraft constrained attitude control using positively invariant constraint admissible sets on SO(3) × R3," *2014 American Control Conference*, 2014, pp. 4955–4960. https://doi.org/10.1109/ACC.2014.6858878.

[18] Frazzoli, E., Dahleh, M., Feron, E., and Kornfeld, R., *A randomized attitude slew planning algorithm for autonomous spacecraft*, Vol. 4155, AIAA Reston, VA, 2001.

[19] Cheng, P., Frazzoli, E., and LaValle, S. M., "Improving the performance of sampling-based planners by using a symmetry-exploiting gap reduction algorithm," *IEEE International Conference on Robotics and Automation, 2004. Proceedings. ICRA'04. 2004*, Vol. 5, IEEE, 2004, pp. 4362–4368.

[20] Calaon, R., and Schaub, H., "Constrained Attitude Maneuvering via Modified-Rodrigues-Parameter-Based Motion Planning Algorithms," *Journal of Spacecraft and Rockets*, Vol. 59, No. 4, 2022, pp. 1342–1356. https://doi.org/10.2514/1.A35294, URL https://doi.org/10.2514/1.A35294.

[21] Calaon, R., Schaub, H., and Trowbridge, M. A., "Basilisk-Based Benchmark Analysis of Different Constrained Attitude Dynamics Planners," *Journal of Aerospace Information Systems*, Vol. 20, No. 2, 2023, pp. 60–69. https://doi.org/10.2514/1.I011109, URL https://doi.org/10.2514/1.I011109.

[22] Weiss, A., Petersen, C., Baldwin, M., Erwin, R., and Kolmanovsky, I., "Safe Positively Invariant Sets for Spacecraft Obstacle Avoidance," *J. of Guidance, Control, and Dynamics*, 2015.

[23] Danielson, C., Weiss, A., Berntorp, K., and Di Cairano, S., "Path Planning using Positive Invariant Sets," *Conf. on Decision and Control*, 2016.

[24] Weiss, A., Danielson, C., Berntorp, K., Kolmanovsky, I., and Di Cairano, S., "Motion Planning with Invariant Set Trees," *Conf. on Control Technology and Applications*, 2017.

[25] Berntorp, K., Weiss, A., Danielson, C., Di Cairano, S., and Kolmanovsky, I., "Automated Driving: Safe Motion Planning using Positive-Invariant Sets," *Intelligent Transportation Systems Conference*, 2017.

[26] Berntorp, K., Bai, R., Erliksson, K. F., Danielson, C., Weiss, A., and Cairano, S. D., "Positive Invariant Sets for Safe Integrated Vehicle Motion Planning and Control," *IEEE Transactions on Intelligent Vehicles*, 2020.

[27] Danielson, C., Berntorp, K., Weiss, A., and Di Cairano, S., "Robust Motion-Planning for Uncertain Systems with Disturbances using the Invariant-Set Motion-Planner," *Accepted to Transactions on Automatic Control*, 2019.

[28] Danielson, C., Berntorp, K., Di Cairano, S., and Weiss, A., "Motion-Planning for Unicycles using the Invariant-Set Motion-Planner," *American Control Conference*, 2020.

[29] Frey, G., Petersen, C., Leve, F., Kolmanovsky, I., and Girard, A., "Constrained Spacecraft Relative Motion Planning Exploiting Periodic Natural Motion Trajectories and Invariance," *J. of Guidance, Control, and Dynamics*, Vol. 12, No. 40, 2017, pp. 3100–3115.

[30] Frey, G., Petersen, C., Leve, F., Kolmanovsky, I., and Girard, A., "Invariance-based Spacecraft Relative Motion Planning Incorporating Bounded Disturbances and Minimum Thrust Constraints," *American Control Conference*, 2017.

[31] Frey, G., Petersen, C., Leve, F., Kolmanovsky, I., and Girard, A., "Incorporating Periodic and Non-Periodic Natural Motion Trajectories into Constrained Invariance-Based Spacecraft Relative Motion," *IEEE Conference on Control Technology and Applications*, 2017.

[32] Danielson, C., Kloeppel, J., and Petersen, C., "Spacecraft Attitude Control using the Invariant-Set Motion-Planner," *IEEE Control Systems Letters*, 2021, pp. 1–1. https://doi.org/10.1109/LCSYS.2021.3132457.

[33] Danielson, C., "Invariant Configuration-Space Bubbles for Revolute Serial-Chain Robots," *IEEE Control Systems Letters*, Vol. 7, 2023, pp. 745–750. https://doi.org/10.1109/LCSYS.2022.3224685.

[34] LaValle, S., and Kuffner, J., "Randomized kinodynamic planning," *The International Journal of Robotics Research*, 2001.

[35] Karaman, S., and Frazzoli, E., "Sampling-based algorithms for optimal motion planning," *Int J of Robotics Research*, Vol. 30, No. 7, 2011, pp. 846–894.

[36] Aubin, J.-P., *Viability Theory*, Birkhauser Boston Inc., 1991.

[37] Leve, F. A., Hamilton, B. J., and Peck, M. A., *Spacecraft Momentum Control Systems*, Springer International Publishing, 2015.

[38] Schwartz, J. L., Peck, M. A., and Hall, C. D., "Historical Review of Air-Bearing Spacecraft Simulators," *J. of Guidance, Control, and Dynamics*, Vol. 26, No. 4, 2003.

[39] Majji, M., Davis, J., Doebbler, J., Junkins, J., Macomber, B., Vavrina, M., and Vian, J., "Terrain mapping and landing operations using vision based navigation systems," *AIAA Guidance, Navigation, and Control Conference*, 2011, p. 6581.

[40] Barari, A., Dion, R., Jeffrey, I., and Ferguson, P., "Testing satellite control systems with drones," *IEEE Potentials*, Vol. 41, No. 1, 2021, pp. 6–13.

[41] Aghili, F., "Coordination control of a free-flying manipulator and its base attitude to capture and detumble a noncooperative satellite," *2009 IEEE/RSJ International Conference on Intelligent Robots and Systems*, 2009, pp. 2365–2372. https://doi.org/10.1109/IROS.2009.5353968.

[42] Zappulla, R., Virgili-Llop, J., Zagaris, C., Park, H., and Romano, M., "Dynamic Air-Bearing Hardware-in-the-Loop Testbed to Experimentally Evaluate Autonomous Spacecraft Proximity Maneuvers," *Journal of Spacecraft and Rockets*, Vol. 54, No. 4, 2017, pp. 825–839. https://doi.org/10.2514/1.A33769, URL https://doi.org/10.2514/1.A33769.

[43] Tsiotras, P., Shen, H., and Hall, C., "Satellite Attitude Control and Power Tracking with Energy/Momentum Wheels," *Journal of Guidance, Control, and Dynamics*, Vol. 24, No. 1, 2001, pp. 23–34. https://doi.org/10.2514/2.4705, URL https://doi.org/10.2514/2.4705.

[44] Wie, B., *Spacecraft Dynamics and Control*, AIAA, 2010.

[45] Park, Y., "Robust and optimal attitude stabilization of spacecraft with external disturbances," *Aerospace Science and Technology*, Vol. 9, No. 3, 2005, pp. 253–259. https://doi.org/https://doi.org/10.1016/j.ast.2005.01.002, URL https://www.sciencedirect.com/science/article/pii/S1270963805000076.

[46] Wie, B., and Lu, J., "Feedback control logic for spacecraft eigenaxis rotations under slew rate and control constraints," *Journal of Guidance, Control, and Dynamics*, Vol. 18, No. 6, 1995, pp. 1372–1379. https://doi.org/10.2514/3.21555, URL https://doi.org/10.2514/3.21555.

[47] Wie, B., Weiss, H., and Arapostathis, A., "Quarternion feedback regulator for spacecraft eigenaxis rotations," *J. of Guidance, Control, and Dynamics*, Vol. 12, No. 3, 1989, pp. 375–380.

[48] Joshi, S., Kelkar, A., and Wen, J.-Y., "Robust attitude stabilization of spacecraft using nonlinear quaternion feedback," *IEEE Transactions on Automatic Control*, Vol. 40, No. 10, 1995, pp. 1800–1803. https://doi.org/10.1109/9.467669.

[49] Grünbaum, B., *Convex polytopes*, Springer, 2003.

[50] Kurokawa, H., "Survey of Theory and Steering Laws of Single-Gimbal Control Moment Gyros," *Journal of Guidance, Control, and Dynamics*, Vol. 30, No. 5, 2007, pp. 1331–1340. https://doi.org/10.2514/1.27316, URL https://doi.org/10.2514/1.27316.

[51] Jones, L. L., Zeledon, R. A., and Peck, M. A., "Generalized Framework for Linearly Constrained Control Moment Gyro Steering," *Journal of Guidance, Control, and Dynamics*, Vol. 35, No. 4, 2012, pp. 1094–1103. https://doi.org/10.2514/1.56207, URL https://doi.org/10.2514/1.56207.

[52] Danielson, C., and Kloeppel, J., "Rapid Construction of Safe Search-Trees for Spacecraft Attitude Planning," *American Control Conference*, 2023.

[53] Das, A., Berg, J. L., Norris, G. A., Cossey, D. F., Strange III, T. J., and Schlaegel, W. T., "ASTREX—A Unique Test Bed for CSI Research," *29th Conference on Decision and Control, 1990.*, IEEE, 1990, pp. 2018–2023.

[54] Keim, J., Behcet Acikmese, A., and Shields, J., "Spacecraft inertia estimation via constrained least squares," *2006 IEEE Aerospace Conference*, 2006, pp. 6 pp.–. https://doi.org/10.1109/AERO.2006.1655995.